

Deformation around neutron-rich Cr isotopes in axially symmetric Skyrme-Hartree-Fock-Bogoliubov method

Hiroshi OBA¹, Masayuki MATSUO²

¹*Graduate School of Science and Technology, Niigata University, Niigata 950-2181, Japan*

²*Department of Physics, Faculty of Science, Niigata University, Niigata 950-2181, Japan*

We analyse deformation mechanism in neutron-rich Cr, Fe and Ti isotopes with $N=32-44$ by means of a Skyrme-Hartree-Fock-Bogoliubov mean-field code employing a two-dimensional mesh representation in the cylindrical coordinate system. Evaluating systematically the quadrupole deformation energy, we show that the Skyrme parameter set SkM* gives a quadrupole instability around the neutron number $N\sim 38-42$ in Cr isotopes, where the deformation energy curve suggests a transitional behavior with a shallow minimum extending to a large prolate deformation. Roles of a deformed $N=38$ gap and the position of the neutron $g_{\frac{3}{2}}$ orbit are analysed in detail.

§1. Introduction

Deformation in the nuclear shape is one of the fundamental features of the nuclear structure. Mechanism of the deformation reflects quantal effects such as the shell effect, the pairing correlation, and the long range proton-neutron correlation. Thus, analyses of a new deformation region often provide us with new insights into nuclear structure. A recent example is the quadrupole deformation in neutron-rich $Z\sim 12$ isotopes, which have been a crucial probe to disclose the weakening of the $N=20$ shell gap in the neutron-rich nuclei.¹⁾ More recently another possibility of a new deformation region has been suggested in neutron-rich Cr isotopes²⁾⁻⁷⁾

The self-consistent mean-field theory is a powerful scheme to analyse the deformation mechanism when we deal with nuclei far from the stability line in medium and heavy mass regions.⁸⁾ There are three important features which should be taken into account in this case: the pairing correlation, the continuum states and the deformation. The pairing correlation can be described by using the Bogoliubov's generalized quasi-particle scheme while the conventional BCS approximation is not suitable for nuclei far from the stability line. The continuum states become important in nuclei near the drip-lines where the Fermi energy becomes close to zero. In this case one has to treat continuum quasi-particle states which have spatially extended wave functions. These two requirements are fulfilled in the Hartree-Fock-Bogoliubov(HFB) formalism once it is represented in the coordinate-space.^{9),10)} To describe the deformation, then, the HFB method has to be extended to a two- or three-dimensional problem, for which several techniques using the truncated Hartree-Fock basis,¹¹⁾⁻¹³⁾ the transformed harmonic oscillator basis,^{14),15)} and the B-Spline basis^{16),17)} have been developed recently.

In the present paper, we develop our own 2D coordinate-space Skyrme-HFB

code, which enables us to describe axially deformed unstable nuclei. The formalism is similar to that of Ref. 16), which utilizes the B-Spline and Galerkin methods on top of the cylindrical coordinate system. In the present approach, we adopt a two-dimensional mesh representation using the cylindrical coordinate system and a multi-points formula for differential operators. Since the 2D mesh approach using the cylindrical coordinate has not been explored except a few Hartree-Fock¹⁸⁾ and Hartree-Fock-Bogoliubov calculations,^{19),20)} we shall test numerical accuracy of our code. Then, as an application of this code, we shall investigate the possible deformation region around the neutron-rich Cr isotopes. A global calculation of the ground state deformation including the neutron-rich Cr isotopes is performed by means of the Skyrme-HFB^{15),21),22)} and the relativistic mean-field models.²³⁾ Here we perform detailed analysis of the deformation mechanism by looking into the deformation energy curve and the shell structure of the single-particle orbits, and dependence on the Skyrme interactions.

§2. The HFB formalism

2.1. The HFB equation in the cylindrical coordinates system

The HFB equation in the coordinate space representation is written as

$$\begin{pmatrix} h_{\sigma\sigma'}^q(\mathbf{r}) - \lambda & \tilde{h}_{\sigma\sigma'}^q(\mathbf{r}) \\ \tilde{h}_{\sigma\sigma'}^q(\mathbf{r}) & -(h_{\sigma\sigma'}^q(\mathbf{r}) - \lambda) \end{pmatrix} \begin{pmatrix} \phi_{\alpha q}^{(1)}(\mathbf{r}\sigma) \\ \phi_{\alpha q}^{(2)}(\mathbf{r}\sigma) \end{pmatrix} = E_{\alpha q} \begin{pmatrix} \phi_{\alpha q}^{(1)}(\mathbf{r}\sigma) \\ \phi_{\alpha q}^{(2)}(\mathbf{r}\sigma) \end{pmatrix} \quad (2.1)$$

assuming the local HF potential $h_{\sigma\sigma'}^q(\mathbf{r})$ and the local pairing potential $\tilde{h}_{\sigma\sigma'}^q(\mathbf{r})$ for neutrons and protons ($q = n$ or p) with σ and σ' being spin indexes ($\sigma, \sigma' = \uparrow, \downarrow$). In the present paper we assume the axial symmetry of nuclear deformation and the z -axis is chosen as the symmetry axis. The quasi-particle wave function has a quantum number Ω for the z -component of the total angular momentum. Using the cylindrical coordinate (r, z, φ) , the quasi-particle wave function of the n -th eigenstate is written as

$$\begin{pmatrix} \phi_{n\Omega q}^{(1)}(\mathbf{r}\sigma) \\ \phi_{n\Omega q}^{(2)}(\mathbf{r}\sigma) \end{pmatrix} = \frac{1}{\sqrt{2\pi}} \begin{pmatrix} e^{i(\Omega-\frac{1}{2})\varphi} \phi_{n\Omega q}^{(1)\uparrow}(r, z) \\ e^{i(\Omega+\frac{1}{2})\varphi} \phi_{n\Omega q}^{(1)\downarrow}(r, z) \\ e^{i(\Omega-\frac{1}{2})\varphi} \phi_{n\Omega q}^{(2)\uparrow}(r, z) \\ e^{i(\Omega+\frac{1}{2})\varphi} \phi_{n\Omega q}^{(2)\downarrow}(r, z) \end{pmatrix}. \quad (2.2)$$

Expressing the Hartree-Fock Hamiltonian $h(r, z, \varphi)$ and the pairing Hamiltonian $\tilde{h}(r, z, \varphi)$ as

$$h^q(r, z, \varphi) = \begin{pmatrix} h_{\uparrow\uparrow}^q(r, z) & e^{-i\varphi} h_{\uparrow\downarrow}^q(r, z) \\ e^{i\varphi} h_{\downarrow\uparrow}^q(r, z) & h_{\downarrow\downarrow}^q(r, z) \end{pmatrix}, \quad (2.3)$$

$$\tilde{h}^q(r, z, \varphi) = \begin{pmatrix} \tilde{h}_{\uparrow\uparrow}^q(r, z) & e^{-i\varphi} \tilde{h}_{\uparrow\downarrow}^q(r, z) \\ e^{i\varphi} \tilde{h}_{\downarrow\uparrow}^q(r, z) & \tilde{h}_{\downarrow\downarrow}^q(r, z) \end{pmatrix}, \quad (2.4)$$

the HFB equation in the cylindrical coordinate representation is written as

$$H_q \Phi_{n\Omega q} = E_{n\Omega q} \Phi_{n\Omega q} \quad (2.5)$$

where

$$H_q = \begin{pmatrix} h_{\uparrow\uparrow}^q(r, z) - \lambda & h_{\uparrow\downarrow}^q(r, z) & \tilde{h}_{\uparrow\uparrow}^q(r, z) & \tilde{h}_{\uparrow\downarrow}^q(r, z) \\ h_{\downarrow\uparrow}^q(r, z) & h_{\downarrow\downarrow}^q(r, z) - \lambda & \tilde{h}_{\downarrow\uparrow}^q(r, z) & \tilde{h}_{\downarrow\downarrow}^q(r, z) \\ \tilde{h}_{\uparrow\uparrow}^q(r, z) & \tilde{h}_{\uparrow\downarrow}^q(r, z) & -h_{\uparrow\uparrow}^q(r, z) + \lambda & -h_{\uparrow\downarrow}^q(r, z) \\ \tilde{h}_{\downarrow\uparrow}^q(r, z) & \tilde{h}_{\downarrow\downarrow}^q(r, z) & -h_{\downarrow\uparrow}^q(r, z) & -h_{\downarrow\downarrow}^q(r, z) + \lambda \end{pmatrix} \quad (2.6)$$

and

$$\Phi_{n\Omega q} = \begin{pmatrix} \phi_{n\Omega q}^{(1)\uparrow}(r, z) \\ \phi_{n\Omega q}^{(1)\downarrow}(r, z) \\ \phi_{n\Omega q}^{(2)\uparrow}(r, z) \\ \phi_{n\Omega q}^{(2)\downarrow}(r, z) \end{pmatrix}. \quad (2.7)$$

We adopt the Skyrme force and $h_{\sigma\sigma'}^q(r, z)$ is expressed¹⁶⁾ in terms of the force parameters and the normal density $\rho_{n,p}(r, z)$, the kinetic density $\tau_{n,p}(r, z)$, the spin-orbit density $J_{n,p}(r, z)$. We adopt the density dependent delta interaction(DDDI)

$$v_{pair} = \frac{1}{2}V_0(1 - P_\sigma) \left(1 - \left(\frac{\rho(\mathbf{r})}{\rho_0} \right)^\eta \right) \delta(\mathbf{r} - \mathbf{r}')$$

for the effective interaction producing the pairing potential $\tilde{h}_{\sigma\sigma'}^q$, where $\tilde{h}_{\sigma\sigma'}^q$ is expressed in terms of the total nucleon density $\rho(r, z)$ and the pair density $\tilde{\rho}_q(r, z)$. The eigenstates and eigenenergies of the quasi-particles are obtained by solving the HFB equation (2.5) for each Ω . Since we assume the time reversal symmetry, we need to solve only for $\Omega > 0$.

We consider a rectangular area $0 \leq r \leq r_{max}$ and $-z_{max} \leq z \leq z_{max}$ in the (r, z) plane. The r -axis is discretized at $r = h/2, 3h/2, \dots, r_{max}$ with N_r mesh points, while the z -axis is discretized from $-z_{max} = -N_z h$ to $z_{zmax} = N_z h$ with the same equidistant interval h . The quasi-particle wave functions $\phi(r, z)$ (the indices are omitted here for simplicity) and the HFB Hamiltonian H_q are represented on this two-dimensional mesh. At the outer boundary $z = \pm z_{max}$ and $r = r_{max}$, we impose $\phi(r_{max}, z) = 0$ and $\phi(r, \pm z_{max}) = 0$. At the origin $r = 0$, we impose $\phi(-r, z) = (-)^{l_z} \phi(r, z)$ determined by the parity $(-)^{l_z}$ where l_z is the z -component of the orbital angular momentum. Note that we utilize shifted mesh points $r = (n + \frac{1}{2})h$ so that we do not need to evaluate the value of ϕ at $r = 0$. We made a comparison with calculations where the r -axis is discretized on a slightly different mesh points $r = 0, h, 2h, \dots, r_{max}$ and we found that the adopted discretization with $r = (n + \frac{1}{2})h$ has better accuracy. We adopt the 11-points formula to represent differential operators. Concerning the integrals, we adopt trapezoidal formula since it is known that the high order formula does not always guarantee a better accuracy.²⁴⁾ Consequently a quasi-particle wave function is expressed as a vector with $N = 4N_z N_r$ dimension and the HFB Hamiltonian is a matrix having the size of N^2 . We obtain the eigenvalues and the eigenfunctions by diagonalizing this Hamiltonian matrix. The Hamiltonian is non-symmetric because of the finite-points representation of the differential operators around $r = 0$. We diagonalize the Hamiltonian using the QR method to solve the non-symmetric eigenvalue problem.

Since we use the delta type pairing force, we introduce a cut-off with respect to the quasi-particle energy. The adopted value of cut-off energy is 60 MeV. We need also a cut-off with respect to the azimuthal quantum number Ω , and we adopted the cut-off value of $\Omega = \frac{15}{2}$. In order to obtain the self-consistent solution, we utilize an iteration scheme. As an initial condition, we start with single-particle orbits in a deformed Woods-Saxon potential. As an initial pairing potential, we chose one having a Woods-Saxon shape. We revise only a fraction of the densities in each step of iteration, and this fraction is randomized within an interval 0.2-0.4. When about 200 iterations pass, the increment of the energy reaches 1×10^{-5} MeV, at which we stop the iteration. In order to obtain a deformation energy, we perform also a constrained HFB calculation. As a constraint operator, we use the mass quadrupole operator \hat{Q}_2 , which is defined as

$$\hat{Q}_2 = \sqrt{\frac{16\pi}{5}} R^2 Y_{20}(\hat{r}) = 2z^2 - r^2$$

($R = \sqrt{r^2 + z^2}$). We use the quadratic constraint method.²⁵⁾

2.2. Test of the numerical code

To check the accuracy of the code, we compare our result with those in the two previous Skyrme-HFB calculations. One is the THO basis method developed by Stoitsov et al.¹⁴⁾ and the other is the B-Spline basis method developed by Terán et al.¹⁶⁾ We choose neutron-rich Zr isotopes. Along with Refs.14) and 16), we adopt the Skyrme parameter SLy4 and the volume type pairing force, *i.e.* $\eta = 0$. The box size is 12 fm for both r_{max} and z_{max} , and the mesh interval h is 0.6 fm. The pairing strength V_0 is the same in Refs. 16) and 17). The obtained ground state properties of neutron-rich Zr isotopes are shown in Table I and Fig.1. The density and the pair

Table I. The total binding energy BE, the Fermi energy λ_q , the average pairing gap Δ_q and the RMS radius $\sqrt{\langle r^2 \rangle}$ in ^{102}Zr obtained in the present work. The values¹⁶⁾ of the B-Spline and the THO methods are compared.

| | present work | B-Spline | THO |
|-----------------------------------|--------------|----------|---------|
| BE [MeV] | -856.92 | -859.61 | -859.40 |
| λ_n [MeV] | -5.42 | -5.46 | -5.42 |
| λ_p [MeV] | -12.07 | -12.08 | -12.10 |
| Δ_n [MeV] | 0.23 | 0.31 | 0.56 |
| Δ_p [MeV] | 0.35 | 0.34 | 0.62 |
| $\sqrt{\langle r^2 \rangle}$ [fm] | 4.58 | 4.58 | 4.58 |

density for neutrons are shown in Fig.1. It is seen that the neutron density has a large quadrupole deformation and the neutron pair density is also deformed. Note that the pair density exhibits a complex structure in the inner region.

In Table I, we compare our result for ^{102}Zr with the results of the B-Spline and the THO methods in Ref. 16). It is seen that our code reproduces reasonably well. Especially, the root mean square (RMS) radius $\sqrt{\langle r^2 \rangle}$ and the Fermi energies $\lambda_{n,p}$ are in a good agreement. Note however that there is a deficiency in the total binding energy by about 2-3 MeV. This is probably due to use of the moderate mesh size

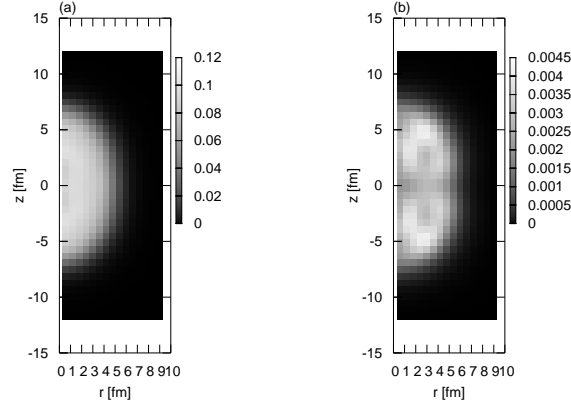


Fig. 1. (a) The density $\rho_n(r, z)$ and (b) the pair density $\tilde{\rho}_n(r, z)$ for neutrons in ^{102}Zr . The unit in the legend is fm^{-3} .

($h=0.6$ fm) and the finite-points formula for the differential operators as a deficiency due to the finite mesh size has been known in previous HF+BCS calculations.^{26),27)} There is some deviation in the average neutron pairing gap Δ_n . It should be noted that the pairing gap is rather small ~ 300 keV. Generally the value of the pairing gap is sensitive to minor differences, especially when the pairing gap is small. A small difference in defining the cut-off energy may be suspected as we adopt the quasi-particle energy cut-off while the THO and B-Spline methods use so called the equivalent single particle energy cut-off. The finite mesh size effect could be another origin.

To make a systematic comparison, we have calculated an isotopic chain of zirconium for $N=102-122$. The mass quadrupole moment Q_2 , the RMS radius, the neutron and proton pairing gaps, and the two-neutron separation energy are compared with those of Ref. 17) in Fig.2(a)-(d). In this calculation, the pairing strength is $V_0=-187.1305$ MeV fm^{-3} . The quadrupole moment (Fig.2(a)) as well as the RMS radius (Fig.2(b)) agree very well with those in the B-Spline and the THO methods in the whole region ($A=102-122$) shown in the figure. Especially the deformation is described well. The difference in the neutron separation energy is smaller than the 2-3 MeV difference in the absolute value of the total binding energy. The better accuracy in the relative quantities is consistent with the same feature found in the previous Skyrme-HF + BCS calculations using the 3D Cartesian mesh representation.²⁸⁾ The average pairing gap is also reproduced reasonably well as shown in Fig.2(c) although a small but non-negligible difference is noted.

In Figure 3, we display the deformation energy curve as a function of the quadrupole deformation parameter β defined by $\beta = \sqrt{\frac{\pi}{5}} \frac{\langle Q_2 \rangle}{\langle r^2 \rangle A}$. The dependence of the quadrupole deformation energy on the mesh size is seen from the comparison of the results obtained with the mesh sizes 0.6 and 0.8 fm. If we shift the total energy by about 1.8 MeV, we see that the difference between the two curves becomes within about 200 keV. We thus conclude that the deformation energy can be evaluated to

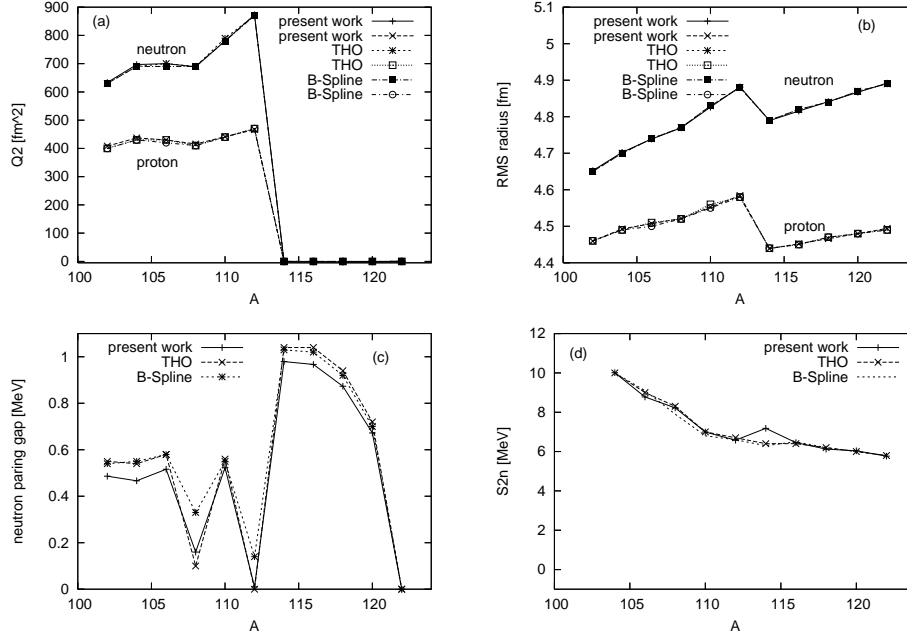


Fig. 2. The comparison of (a) the mass quadrupole moment Q_2 , (b) the RMS radius $\sqrt{\langle r^2 \rangle}$, (c) the neutron average pairing gap Δ_n , and (d) the two neutron separation energy S_{2n} in the neutron-rich Zr isotopes between the present work and the B-Spline and the THO methods.¹⁷⁾

the accuracy of this order.

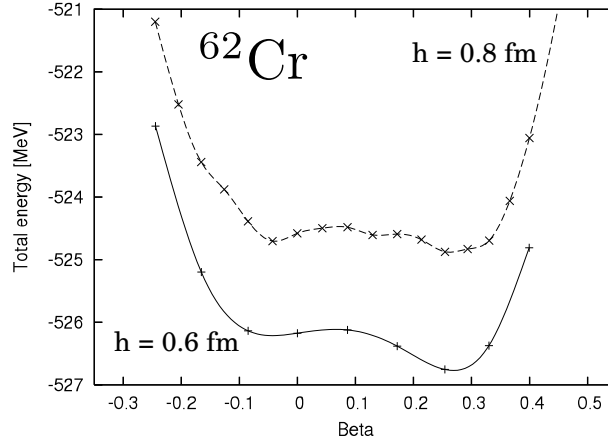


Fig. 3. The deformation energy curves as a function of the deformation parameter β calculated for ^{62}Cr using SkM*. The solid line is the case of $h = 0.6$ fm and the dash line for 0.8 fm.

§3. Quadrupole deformation around the neutron-rich Cr isotopes with $N \sim 38$

3.1. The neutron-rich Cr isotopes and neutron single-particle gaps

The observed 2_1^+ energy of the neutron-rich Cr isotopes decreases monotonically with increasing the neutron number from $E_2 = 1007$ keV in ^{56}Cr down to 446 keV in ^{62}Cr ,²⁾ suggesting a new region of deformation. The energy ratio E_4/E_2 between the 2_1^+ and 4_1^+ excited states becomes large $E_4/E_2=2.65$ in ^{62}Cr ⁷⁾ while the ratio is small $E_4/E_2 \sim 2.2$ for lighter isotopes.⁶⁾ The proton inelastic scattering experiment⁷⁾ indicates that the 2_1^+ state accompanies a large quadrupole deformation $\beta \sim 0.25$. Shell model analyses^{2),29)} suggest a possible deformation for $N \geq 38$ as an extended model space including at least the neutron $1g_{7/2}$ and $2d_{5/2}$ orbits in the higher shell is necessary to describe the decreasing trend of E_2 with increasing the neutron number. There are several self-consistent mean-field calculations^{21)–23)} for the systematics of the ground state deformation, including the neutron-rich Cr isotopes. The calculation using the Skyrme parameter set SkM*²¹⁾ produces a large prolate deformation around ^{62}Cr , but the other Skyrme models using SLy4,²¹⁾ SkP,²¹⁾ BSk2²²⁾ and the relativistic mean-field model using NL-SH²³⁾ do not. Here we analyse the microscopic deformation mechanism with focuses on the parameter set SkM*.

First, we discuss the deformation energy curve in $^{56-68}\text{Cr}$. We adopt SkM* and

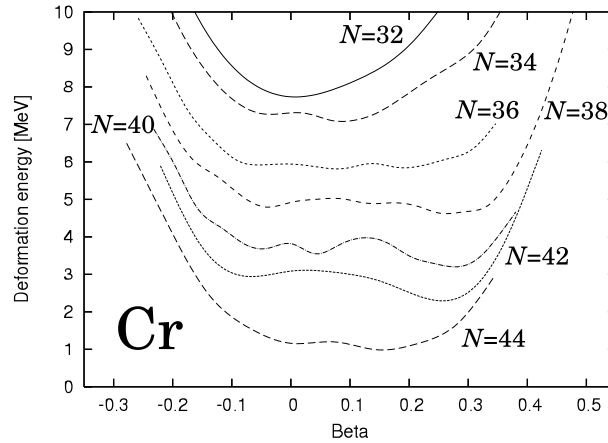


Fig. 4. The quadrupole deformation energy curves of the neutron-rich Cr isotopes calculated with SkM*. The energy is arbitrarily shifted for the sake of comparison.

the volume type pairing force ($\eta = 0$ in (2.1)) with the pairing strength $V_0 = -200$ MeV fm⁻³. The value of V_0 is adjusted to reproduce the odd-even mass difference in $^{56-66}\text{Cr}$, which have the values between 1.5 and 2.0 MeV. The ground state values of β , Δ_n and Δ_p are shown in Table II. The calculated deformation energy curves of the neutron-rich Cr isotopes are plotted in Fig.4. It is seen that the deformation energy curve becomes soft toward the prolate direction with increasing the neutron number from $N=32$. In ^{60}Cr the deformation energy is almost flat between $\beta=-0.1$ and 0.3. In $^{62,64,66}\text{Cr}$ ($N=38-42$), the minimum with a large quadrupole deformation

appears around $\beta=0.25 - 0.3$, but then the deformation of the minimum decreases for $N \geq 42$. The calculated isotopic tendency is consistent with the observed trend of E_2 from $N=32$ to $N=38$. It is noted, however, that the energy difference between the spherical configuration($\beta=0$) and the quadrupole deformed minimum is small. In the case of ^{62}Cr , the difference is about 290 keV. If we estimate the zero-point energy in terms of the experimental value of $E_2=446$ keV, the deformation energy and the zero-point energy have comparable magnitudes. Thus it is suggested, within the SkM* model, that even in $^{62-64}\text{Cr}$ exhibiting the largely deformed minima a well developed static deformation is not realized, and that a large amplitude quadrupole motion of a transitional character is expected. The transitional nature seems to be consistent with the observed E_4/E_2 ratio⁷⁾ 2.65 in ^{62}Cr which lies in between the vibrator and the rotor limits 2 and 3.33.

Next we analyse the mechanism of the deformation. For this purpose, we plot the Hartree-Fock single-particle energies as a function of β . The single-particle orbits are obtained by re-diagonalizing the HF Hamiltonian associated with the constrained Skyrme-HFB solution. The result is shown in Fig.5(a) and (b). The neutron subshell

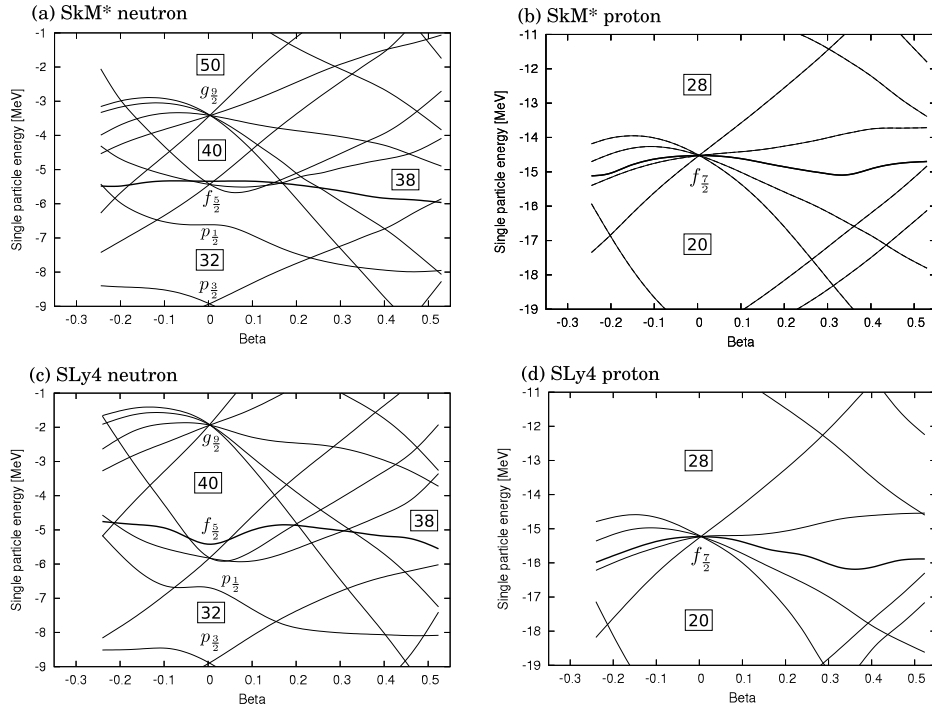


Fig. 5. The single-particle energies obtained with SkM*(left panels (a)(b)) and SLy4(right panels (c)(d)) for ^{62}Cr . The top panels (a)(c) are for neutrons, and the bottom panels (b)(d) are for protons. The thick solid line is the Fermi energy. The horizontal axis is the quadrupole deformation parameter β .

gap $N=40$ between the $f_{7/2}$ and $g_{7/2}$ orbits in the spherical region and an energy gap $N=38$ in the prolate region around $\beta=0.25-0.5$ are notable. As the magnitude of the deformed $N=38$ gap is comparable to the spherical $N=40$ subshell gap, it is

easy to deduce that the deformed $N=38$ gap may drive the nucleus toward prolate deformation with $\beta \sim 0.3$. We also note that the neutron $g_{\frac{9}{2}}$ orbit plays an important role in forming the deformed states. Especially the $\Omega = \frac{1}{2}$ and $\frac{3}{2}$ orbits which stem from the deformation splitting of $\nu g_{\frac{9}{2}}$ are relevant as they exhibit the steepest down-sloping for $\beta \geq 0$. If neutrons occupy these $\nu g_{\frac{9}{2}}$ orbits, they cause a strong driving force toward prolate deformation. This situation can be realized for $\beta \gtrsim 0.20$. We show in Table II the occupation number for all of the $\nu g_{\frac{9}{2}}$ orbits. The occupation number ~ 3.0 - 3.8 in ^{62}Cr and ^{64}Cr , where the largest ground state deformation is realized, is consistent with the interpretation that the $\nu g_{\frac{9}{2}}$ $\Omega = \frac{1}{2}$ and $\frac{3}{2}$ orbitals are largely occupied. As the neutron number goes beyond $N=38$, the occupation number of $\nu g_{\frac{9}{2}}$ still increases slightly (3.8 in ^{64}Cr with $N=40$ and 4.4 in ^{66}Cr with $N=42$). However, the quadrupole deformation then turns to decrease at $N=42$ since the upsloping orbits $[303 \frac{5}{2}]$ and $[301 \frac{1}{2}]$ stemming from $\nu f_{\frac{5}{2}}$ and $\nu p_{\frac{1}{2}}$ are occupied. This explains the reason for the largest quadrupole deformation in $^{62,64}\text{Cr}$ with $N=38$ - 40 . The important role of the occupation of $\nu g_{\frac{9}{2}}$ is consistent with the conclusions of the shell model analyses.^{2),3),6),29)}

3.2. Neutron-rich Ti and Fe isotopes

It is interesting to investigate neutron-rich Fe and Ti isotopes around $^{62,64}\text{Cr}$ with $N=38, 40$ with which the largest deformation is realized in the Cr isotopes. Figure 6 shows the deformation energy curve calculated with SkM* for the $N=38$ isotones ^{60}Ti , ^{62}Cr , ^{64}Fe and for the $N=40$ isotones ^{62}Ti , ^{64}Cr , ^{66}Fe . It is seen that

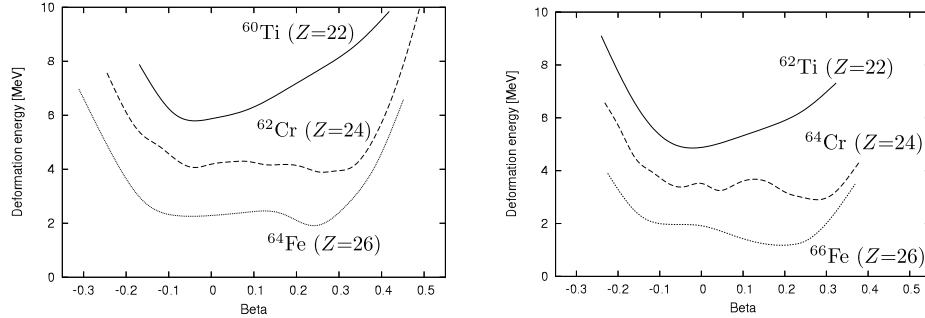


Fig. 6. The quadrupole deformation energy curves of the neutron-rich $N=38$ and 40 isotones around $Z=24$ obtained with SkM*.

the Cr and Fe isotopes have deformed minima at prolate deformation while the Ti isotopes do not exhibit this feature. Since the importance of proton configurations is easily inferred, we look into the proton Nilsson diagram in Fig.5(b), which is for ^{62}Cr but essentially the same for the nuclei under discussion. We also show the occupation number in the proton $f_{\frac{7}{2}}$ orbits in Table II. The occupation numbers are $\sim 2, 4$, and 6 in Ti, Cr and Fe respectively as naturally expected from Fig.5(b). Since the $\Omega = \frac{1}{2}$ and $\Omega = \frac{3}{2}$ orbits stemming from $\pi f_{\frac{7}{2}}$ have steep slopes in the prolate direction, simultaneous occupation of these orbits in Cr gives a large driving

Table II. The occupation numbers of the neutron $g_{\frac{5}{2}}$ orbit and the proton $f_{\frac{7}{2}}$ orbit, the average neutron and proton pairing gaps Δ_n , Δ_p and the quadrupole deformation parameter β associated with the HFB solutions obtained with SkM*.

| | neutron $g_{\frac{5}{2}}$ | proton $f_{\frac{7}{2}}$ | Δ_n [MeV] | Δ_p [MeV] | β |
|------------------|---------------------------|--------------------------|------------------|------------------|---------|
| ^{60}Ti | 1.28 | 2.02 | 2.042 | 1.198 | 0.0 |
| ^{62}Ti | 1.28 | 2.02 | 2.096 | 1.157 | 0.0 |
| ^{58}Cr | 0.355 | 3.98 | 1.619 | 1.427 | 0.0 |
| ^{60}Cr | 0.794 | 3.98 | 1.970 | 1.388 | 0.0 |
| ^{62}Cr | 2.98 | 4.00 | 1.908 | 0.405 | 0.257 |
| ^{64}Cr | 3.85 | 4.02 | 1.904 | 0.212 | 0.262 |
| ^{66}Cr | 4.39 | 4.00 | 1.833 | 0.280 | 0.247 |
| ^{68}Cr | 5.40 | 4.00 | 1.756 | 0.456 | 0.222 |
| ^{64}Fe | 2.58 | 5.99 | 1.999 | 0.280 | 0.212 |
| ^{66}Fe | 3.76 | 6.00 | 1.951 | 0.008 | 0.231 |

force toward the prolate deformation. We can expect that the deformation is a less favored in Fe than in Cr because protons in Fe occupy the $\Omega = \frac{5}{2}$ orbits which is slightly up-sloping. Indeed the value of β at the minima in $^{64,66}\text{Fe}$ is little smaller than those in $^{62,64}\text{Cr}$ (cf. Table II, Fig.6). On the other hand the spherical minima in Ti isotopes indicate that occupation of the $\Omega = \frac{1}{2}$ orbit alone is not enough to cause deformation.

The observed 2_1^+ energies³⁰⁾ in $^{64,66}\text{Fe}$ are lower than that in ^{62}Fe , and the observed ratio³¹⁾ $E_4/E_2=2.36$ in ^{64}Fe is smaller than that(=2.65) in ^{62}Cr .⁷⁾ The deformation energy curves indicating smaller quadrupole deformation in $^{64,66}\text{Fe}$ than in $^{62,64}\text{Cr}$ are consistent with these experimental trends. In addition, the calculation predicts much less collectivity in Ti than in Cr and Fe isotopes. This is also consistent with higher E_2 in ^{58}Ti than in ^{60}Cr .⁷⁾

3.3. Relation to the $N \sim Z=38-40$ deformed region

The role of the $N=38$ deformed shell gap reminds us of the mechanism of the prolate deformation in proton-rich Sr and Zr isotopes with $N \sim Z=38-40$ as the large deformation in the proton-rich $N=Z$ region originates from the presence of a deformed shell gap at $N, Z=38$ and 40 around $\beta \sim 0.4$.^{26), 32), 33)} It is therefore interesting to investigate how the deformation of the neutron-rich Cr, Fe nuclei is related to the $N \sim Z=38-40$ cases. Figure 7 compares the deformation energy curve in ^{62}Cr with those of $^{68}\text{Zn}(Z=30)$ and $^{76}\text{Sr}(Z=38)$ in the $N=38$ isotone chain up to $N=Z=38$. Note that the deformation energy curve in the $N=Z=38$ nucleus ^{76}Sr has a well-developed deformed minimum around $\beta \sim 0.4$.

Figure 8 plots the neutron Nilsson diagram in ^{76}Sr . (The proton Nilsson diagram is not shown here as it is very similar to the neutron's except an overall energy shift due to the Coulomb potential.) Comparing the neutron Nilsson diagrams in Fig.8 and in Fig.5 (a), we see that the presence of the deformed $N=38$ gap is common to both cases. The $N=38$ deformed gap at $\beta \sim 0.4$ is universal in the sense that it exist both in the proton-rich and the neutron-rich regions. This confirms that the deformation mechanism in the neutron-rich Cr and Fe isotopes is intimately related

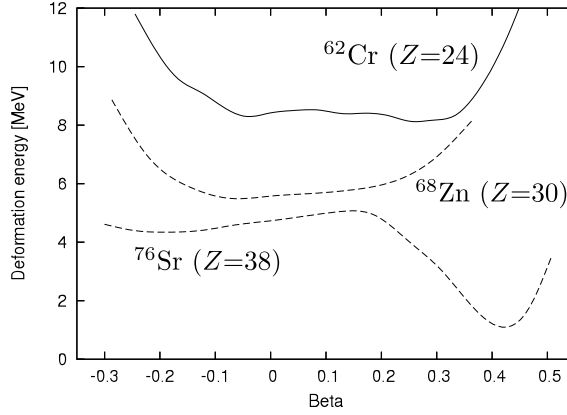


Fig. 7. The quadrupole deformation energy curves in the $N=38$ isotones obtained with SkM*.

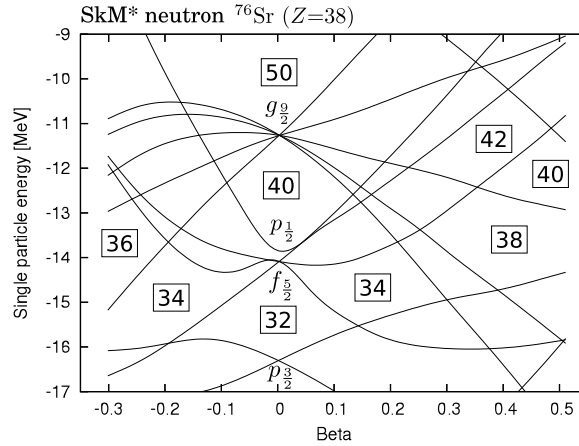


Fig. 8. The neutron Nilsson diagram of ^{76}Sr obtained with SkM*.

to that in the $N=Z \sim 38$ region.

In spite of the above similarity, however, there is small but clear differences between the neutron Nilsson diagrams in the proton-rich $N=Z \sim 38$ region and in the neutron-rich Cr-Fe region. Looking closely at the $N=38$ deformed shell gap, we see that the relevant level crossing of the down-sloping $\nu g_{9/2}^-$ $\Omega = \frac{3}{2}$ orbit and the up-sloping orbit from $\nu f_{5/2}^-$ and $\nu p_{1/2}^-$ occurs at smaller deformation $\beta \sim 0.20$ in the neutron-rich ^{62}Cr than in ^{76}Sr , where the crossing takes place at $\beta \sim 0.26$. It is also seen that the $N=40$ spherical gap at $\beta \sim 0$ is smaller in the neutron-rich ^{62}Cr than in ^{76}Sr . Both features are helpful to produce a largely deformed minimum at $\beta \sim 0.27$ in the deformation energy curve of ^{62}Cr even though the deformation driving effect due to the proton configuration is weaker in ^{62}Cr than in ^{76}Sr . Note also that the deformed shell gap at $N=40$ around $\beta \sim 0.45$ present in ^{76}Sr is barely seen in ^{62}Cr . Another difference is also seen in the $N=34$ oblate gap which is large in the proton-rich region (cf. Fig.8), leading to an oblate ground state in ^{68}Se ($\beta = -0.21$).^{13),32),34)} However the $N=34$ oblate gap is much weaker in the neutron-

rich Cr isotopes(Fig.5(a)), and hence the deformation energy curve in ^{58}Cr (Fig.4) does not show very strong tendency toward the oblate deformation.

3.4. Interaction dependence

As we have seen above, the Skyrme-HFB model using the parameter set SkM* produces the onset of large quadrupole deformation in the $N \sim 38\text{-}40$ region of the Cr isotopes, being in qualitative agreement with the experimental observations. It is noted however that the calculations using other parameter sets such as SLy4, SkP²¹⁾ and BSk2²²⁾ do not show largely deformed minima in the same isotopes. Let us discuss how the onset of deformation depends on the Skyrme parameter sets by comparing results which we obtain using SLy4 as well as SkM*. The calculation for SLy4 is the same as above except for the use of different Skyrme parameters. We show in Fig.9 the deformation energy curve in ^{62}Cr obtained with the parameter set SLy4. The deformation energy curve for SLy4 does not have a well deformed

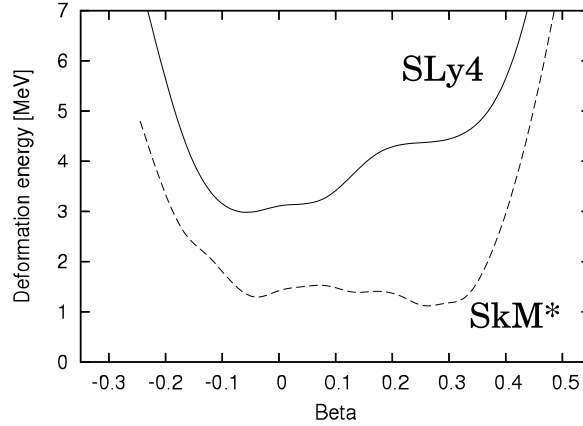


Fig. 9. The deformation energy curve obtained with SLy4 in ^{62}Cr , plotted with the solid curve. The one for SkM* is also shown with the dotted curve for comparison.

minimum, and it is stiff with respect to the quadrupole deformation. We show the neutron Nilsson diagram for SLy4 in Fig.5 (c). By comparing with the Nilsson diagram for SkM* (Fig.5 (a)), we see a large difference in the position of the $\nu g_{\frac{9}{2}}$ orbit. The $N=40$ subshell gap at the spherical point is larger in the case of SLy4 than SkM* by about 2 MeV. The higher position of $\nu g_{\frac{9}{2}}$ also shifts the position of the $N=38$ deformed single-particle gap at larger deformation $\beta > 0.35$ in the SLy4 case. These features apparently favor the stability of the spherical shape in contrast to the case of SkM*. All these observations indicate that the position of the $g_{\frac{9}{2}}$ orbit plays a central role for the onset of the quadrupole deformation in the neutron-rich Cr and Fe isotopes around $N=38$. The precise position of the $\nu g_{\frac{9}{2}}$ orbit and the size of the $N=40$ subshell gap depend on the Skyrme parameter set. In other words, the deformation properties in the neutron-rich Cr region provides us with a rather strong constraint for a proper choice of the Skyrme parameter set.

§4. Conclusions

We have developed an axially symmetric Skyrme-HFB code based on the 2D mesh representation in the cylindrical coordinate system in order to describe the quadrupole deformation of unstable nuclei. Our code has enough accuracy to analyse the deformation property as tested by comparisons with the calculations using the THO and the B-Spline methods.

We applied the code to neutron-rich Cr, Fe and Ti isotopes around a possible new region of deformation with $N \gtrsim 38$. The quadrupole deformation energy curve obtained with the Skyrme parameter set SkM* indicates an onset of deformation in the isotopes with $N \sim 38-42$. The deformation energy curve is soft although the deformation of the minimum reaches $\beta \sim 0.25$ for $N=38$ and 40, and hence the nuclei in this region are expected to exhibit strong quadrupole collectivity having transitional character rather than that associated with a well developed stable deformation. These results are in qualitative agreement with the trends of the presently available experimental data. The SkM* model describes also the Fe isotopes in the same mass region as transitional nuclei while the Ti isotopes are described as spherical nuclei having stiffer quadrupole deformation energy curve. By inspecting the neutron Nilsson diagram we discussed that the deformed $N=38$ gap emerging at $\beta \gtrsim 0.25$ as well as the position of $\nu g_{\frac{9}{2}}$ orbit play important role for the onset of quadrupole deformation. We have also shown that, contrary to SkM*, the parameter set SLy4 is not able to reproduce the onset of deformation. The sensitivity to the Skyrme parameter set arises from the fact that the deformation in this region emerges as a consequence of a delicate competition between spherical and deformed configurations, for which the position of $\nu g_{\frac{9}{2}}$ orbit plays an essential role.

Acknowledgements

This work was supported by the Grant-in-Aid for Scientific Research(No.17540244) from the Japan Society for the Promotion of Science, and also by the JSPS Core-to-Core Program, International Research Network for Exotic Femto Systems(EFES). The numerical calculations were carried out partly on SX8 at YITP in Kyoto University.

References

- 1) T. Motobayashi et al., Phys. Lett. B **346** (1995), 9.
- 2) O. Sorlin et al., Eur. Phys. J. A **16** (2003), 55.
- 3) S. J. Freeman et al., Phys. Rev. C **69** (2004), 064301.
- 4) A. N. Deacon et al., Phys. Lett. B **622** (2005), 151.
- 5) A. N. Deacon et al., Phys. Lett. B **625** (2005), 375.
- 6) S. Zhu et al., Phys. Rev. C **74** (2006), 064315.
- 7) N. Aoi et al., Nucl. Phys. A in press.
- 8) M. Bender, P. -H. Heenen, P. -G. Reinhard, Rev. Mod. Phys. **75** (2003), 121.
- 9) J. Dobaczewski, H. Flocard, J. Treiner, Nucl. Phys. A **422** (1984), 103.
- 10) A. Bulgac, preprint FT-194-1980, Bucharest, 1980, nucl-th/9907088.
- 11) B. Gall, P. Bonche, J. Dobaczewski, H. Flocard and P. -H. Heenen, Z. Phys. A **348** (1994), 183.

- 12) J. Terasaki, P. -H. Heenen, H. Flocard, P. Bonche, Nucl. Phys. A **600** (1995), 371.
- 13) M. Yamagami, K. Matsuyanagi, M. Matsuo, Nucl. Phys. A **693** (2001), 579.
- 14) M. V. Stoitsov, J. Dobaczewski, P. Ring, and S. Pittel, Phys. Rev. C **61** (2000), 034311.
- 15) M. V. Stoitsov, J. Dobaczewski, W. Nazarewicz, S. Pittel, D. J. Dean, Phys. Rev. C **68** (2003), 054312.
- 16) E. Terán, V. E. Oberacker, A. S. Umar, Phys. Rev. C **67** (2003), 064314.
- 17) A. Blazkiewicz, V. E. Oberacker, A. S. Umar, M. Stoitsov, Phys. Rev. C **71** (2005), 054321.
- 18) P. Hoodbhoy, J. W. Negele, Nucl. Phys. A **288** (1977), 23.
- 19) K. Yoshida, M. Yamagami, K. Matsuyanagi, Nucl. Phys. A **779** (2006), 99.
- 20) K. Yoshida, N. V. Giai, nucl-th/0802.1687v1.
- 21) J. Dobaczewski, M. V. Stoitsov, W. Nazarewicz, AIP Conference Proceedings **726** (2004), 51 ed. R. Bijker, R. F. Casten, A. Frank, Skyrme-HFB deformed nuclear mass table, available at <http://www.fuw.edu.pl/~dobaczew/thodri/thodri.html>.
- 22) S. Goriely, M. Samyn, P. H. Heenen, J. M. Pearson, F. Tondeur, Phys. Rev. C **66** (2002), 024326 and IAEA RIPL-2 Reference Input Parameter Library(<http://www-nds.iaea.org/RIPL-2/>)
- 23) G. A. Lalazissis, A. R. Farhan, M. M. Sharma, Nucl. Phys. A **628** (1998), 221.
- 24) N. Tajima, Prog. Theor. Phys. Suppl. No. 142 (2001), 265.
- 25) P. Ring and P. Schuck, *The Nuclear Many-Body Problem* (Springer-Verlag, New York, 1980).
- 26) P. Bonche, H. Flocard, P. H. Heenen, Nucl. Phys. A **443** (1985), 39.
- 27) D. Baye, P. -H. Heenen, J. Phys. A **19** (1986), 2041-2059.
- 28) N. Tajima, Phys. Rev. C **69** (2004), 034305.
- 29) E. Caurier, F. Nowacki, A. Poves, Eur. Phys. J. A **15** (2002), 145-150.
- 30) M. Hannawald et al., Phys. Rev. Lett. **82** (1999), 1391.
- 31) N. Hoteling et al., Phys. Rev. C **74** (2006), 064313.
- 32) W. Nazarewicz, J. Dudek, R. Bengtsson, T. Bengtsson and I. Ragnarsson, Nucl. Phys. A **435** (1985), 397.
- 33) K. Heyde, J. Moreau, M. Waroquier, Phys. Rev. C **29** (1984), 1859.
- 34) S. M. Fischer et al., Phys. Rev. Lett. **84** (2000), 4064.